In situ synthesis of TiO$_2$@NH$_2$-MIL-125 composites for use in combined adsorption and photocatalytic degradation of formaldehyde

Qianqian Huang[a], Yun Hu[a,b,c,*], Yun Pei[a], Jinhui Zhang[a], Mingli Fu[a,b,c]

[a] School of Environment and Energy, South China University of Technology, Guangzhou 510006, PR China
[b] Guangdong Provincial Key Laboratory of Atmospheric Environment and Pollution Control, Guangzhou 510006, PR China
[c] The Key Lab of Pollution Control and Ecosystem Restoration in Industry Clusters, Ministry of Education, Guangzhou 510006, PR China

ARTICLE INFO

ABSTRACT

TiO$_2$@NH$_2$-MIL-125, composite photocatalysts with close interfacial contact between NH$_2$-MIL-125 and TiO$_2$, were successfully synthesized via an in-situ solvothermal method for formaldehyde (HCHO) removal under UV irradiation. Samples were characterized by using a variety of analytical techniques. The results showed that TiO$_2$ particles were highly dispersed on the surface of NH$_2$-MIL-125, and there was a strong electronic interaction (Ti-N-C) between elements of the composite. TiO$_2$@NH$_2$-MIL-125 exhibited significantly enhanced photocatalytic performance for HCHO removal compared to pure TiO$_2$ and NH$_2$-MIL-125 that was ascribed to the synergistic combination of high adsorption capacity of NH$_2$-MIL-125, high dispersion of TiO$_2$ and efficient interfacial charge transfer between TiO$_2$ and NH$_2$-MIL-125. Furthermore, the HCHO removal rate over the composite remained at 90% after 122 h of continuous photocatalytic reaction, indicating the high stability of the catalyst. This work provides new insights that will be helpful in the further development of photocatalysts for indoor air purification.

1. Introduction

Indoor air quality (IAQ) is an important factor affecting human health because people often spend more time indoors than they do outdoors. Poor IAQ can result in serious health problems and economic losses. Formaldehyde (HCHO) is a typical indoor volatile organic compounds (VOC) that can cause "sick building syndrome" [1,2]. The International Agency for Research on Cancer (IARC) has categorized HCHO as a human carcinogen (Group 1) [3]. The compound ranks second on the priority list of toxic chemicals in China. Therefore, it is not surprising that various efforts have been made to eliminate HCHO in order to comply with stringent environmental laws and regulations to protect human health. Although air purifiers are widely used in indoor air purification, these devices simply adsorbed HCHO onto the filter medium (e.g., activated carbon) but do not degrade the pollutant. As a result, the success of air purifiers are limited by low adsorption capacity, re-release of the gas into the air and difficulty in regenerating the adsorbent [4,5]. Hence, there is a need to develop a lower cost, more efficient and more environmentally friendly way of eliminating low concentration levels of HCHO from the air. Photocatalytic oxidation (PCO), as a most promising technology for removal of HCHO because it removes the pollutant and oxidizes it to CO$_2$ and H$_2$O [2,5–8].

TiO$_2$ is a widely used photocatalyst due to its biological and chemical inertness, strong oxidizing power, low cost-effectiveness ratio, and long-term stability against photocorrosion and chemical corrosion [4,9–12]. However, serious problems remain that hinder its application in air purification. For example, pure TiO$_2$ particles tend to aggregate, resulting in poor adsorption capacity and low utilization of active sites [13,14]. The fast recombination of photogenerated carriers within agglomerated TiO$_2$, which results in low photocatalytic activity [13–16]. One strategy to overcome these limitations is to load TiO$_2$ onto a porous material with a high surface area. Such structure can effectively disperse the photoactive phase, improve the separation of the photo-generated carriers, and allow the adsorption of the target pollutant in the vicinity nearby the photocatalytic reaction sites [14,17–19]. Following this strategy, researchers have developed such adsorbent-photocatalyst hybrids that are promising bifunctional immobilized photocatalysts that target removal and destruction of airborne VOCs. In efforts to find more effective VOCs adsorbents, many materials have been studied as supports for TiO$_2$, such as carbon materials, natural silicates, zeolites and molecular sieves. However, they cannot effectively accelerate the charge transfer of samples. In addition, these materials have low adsorption capacity for HCHO, and some of them create secondary pollution [20]. Moreover, many studies are now carried out in static

reaction systems, but continuous flow condition is more suitable for real air treatment systems. Zhang el al. reported that the conversion of HCHO over the TiO_2/zeolite composite was 83% in a static photocatalytic reaction system [21]. Zhu et al. reported that the photocatalytic HCHO oxidation over plasmonic Au/TiO_2 showed 88% of conversion in a dynamic reaction system, while the mineralization of HCHO into CO_2 was very low (about 35%) [6]. Therefore, it is important to find a material that has good adsorption capacity for HCHO, can promote the dispersion of TiO_2 and can improve the separation efficiency of photogenerated carriers in a continuous flow condition. This paper reports on our efforts to achieve these goals.

Recently, metal-organic-frameworks (MOFs) have received considerable attention as a new type of porous material has received great attention. MOFs are composed of metal-oxo clusters and organic ligands that have been studied in range of applications (e.g., CO_2 conversion, hydrogen production, gas storage/separation and heterogeneous catalysis) due to their advantages of large surface area, tunable pore size, large pore volume and adjustable chemistry [22–26]. As a result, MOFs are promising candidates for HCHO adsorption and degradation due to their high surface area and microporosity and their properties as semiconductors. In order to improve the photocatalytic activity of TiO_2 for HCHO removal, we can functionally integrate VOCs adsorption into the MOFs and complex it with TiO_2. NH_2-MIL-125 is an MOF made of Ti_8O_8 ring-shaped cluster and 2-aminoterephtalic acid, which is expected to bring additional advantages in adsorption and catalysis [27]. In addition to its large specific surface area and microporous structure, abundant amine groups and hydrophilic surface are speculated to enhance the adsorption of HCHO. NH_2-MIL-125 is also relatively inexpensive, non-toxic, and water-/photo-stable. To the best of our knowledge, the synergistic adsorption-photocatalytic degradation of gaseous HCHO on NH_2-MIL-125 combined with TiO_2 has not been previously reported.

The purpose of this study is to use a complex structure of MOFs with TiO_2 to form composite materials for photocatalytic removal of HCHO from the vapor phase. Composites of TiO_2 and NH_2-MIL-125 with different ratios of TiO_2 were fabricated through a hydrothermal method using $TiCl_4$ as the titanium source of the MOFs. The properties of the composite materials were investigated by various analytical techniques, and then the adsorption-photocatalytic degradation of HCHO was studied. The possible mechanism of the significant HCHO removal was also investigated.

2. Experimental

2.1. Materials

Titanium tetrachloride (Sinoharm Chemical Reagent Co.,Ltd, AR), 2-aminoterephtalic acid (Sigma-Aldrich, AR), titanium tetraisopropanolate (Aladdin, AR), terephthalic acid (Macklin, AR), methanol and *N,N*-dimethylformamide (Damao Chemical Reagent Factory, AR), sodium sulfate and sodium hydroxide (Aladdin, AR), Degussa P25 (containing 80% anatase and 20% rutile) and formaldehyde (Macklin, AR) were used without further purification.

2.2. Preparation of samples

The $TiO_2@NH_2$-MIL-125 composites were synthesized by a solvothermal method. Typically, a certain amount of TiO_2 was dispersed into a mixture containing 40 mL of *N,N*-dimethylformamide (DMF) and 10 mL of methanol (MeOH). After 30 min, 2.905 g of 2-aminterephtalic acid and 1 mL of $TiCl_4$ were added to above mixture until 2-aminoterephtalic acid was completely dissolved. Then the mixture was

transferred to a Teflon-lined stainless-steel autoclave at 110 °C for 72 h. After cooling to room temperature, the solid product was washed with DMF and MeOH and dried at 100 °C for 12 h. The additive mass of TiO_2 was equal to the total weight of the two important precursors ($TiCl_4$ and 2-aminoterephtalic acid) of NH_2-MIL-125, which mass ratio were 0.1:1, 0.2:1, 0.3:1, and 0.4:1, respectively. The actual content of TiO_2 in the $TiO_2@NH_2$-MIL-125 composites determined by thermogravimetric analysis (TGA) were 24 wt%, 38 wt%, 46 wt% and 54 wt%, respectively. The obtained samples were marked as 24TiO2@76NM, 38TiO2@62NM, 46TiO2@54NM, 54TiO2@46NM. NH_2-MIL-125 was synthesized with above method without TiO_2 added.

For comparison, 46TiO2/54NM-Mech and 46TiO2/54NM-Evap were prepared by mechanical grinding and solvent evaporation methods, respectively. 46TiO2/54NM-Mech was obtained by adding 0.069 g of TiO_2 and 0.081 g of pure NH_2-MIL-125 to a mortar and grinding by hand. 46TiO2/54NM-Evap was prepared by mixing 0.069 g of TiO_2 and 0.081 g of pure NH_2-MIL-125 in 20 mL of methanol, and then sonicated for 30 min, stirred for 12 h and dried at 100 °C for 12 h. MIL-125 was obtained by a typical solvothermal method. 1.6 mL of titanium tetraisopropanolate and 3.009 g terephthalic acid were dissolved in a mixture containing 56 mL of DMF and 6 mL of MeOH. And then the mixture was transferred to a Teflon-lined stainless-steel container and autoclaved at 150 °C for 48 h. After the reaction, the resultant suspension was washed with DMF and MeOH and dried at 100 °C for 12 h.

2.3. Characterization

The crystalline structure of the samples was examined by X-ray diffraction (XRD, D8 Advance diffractometer, Cu Kα radiation, λ = 1.540598 Å). The samples were analyzed over a 2θ range from 5° to 80°. The functionalized groups of samples were characterized by Fourier-transformed infrared spectra (FT-IR, Nicolet-6700 FT-IR spectrometer) using KBr pellets. The atomic compositions of the samples were measured by X-ray photoelectron spectroscopy (XPS, Thermo Fisher Scientific, ESCALAB 250) with Al Kα source. The Raman spectra were recorded with a Raman spectroscopy in the range of 100˜4000 cm^{-1} under a 785 nm diode laser excitation. The images of the morphology and structure of the samples were obtained from scanning electron microscopy (SEM, Nova Nano SEM 430, USA). Diffuse reflectance UV–vis spectroscopic measurements were performed with a Shimadzu UV–vis spectrophotometer UV-2550, using $BaSO_4$ as a reference sample. The specific surface area of samples were obtained from N_2 adsorption-desorption isotherms at 77 K (MICROMERITICS ASAP 2020 M Analysis). Thermogravimetric analysis (TGA) was carried out under a nitrogen flowrate of 10 mL·min^{-1}, from 30 to 600 °C at a heating rate of 10 °C min^{-1} using a Netzsch TG 209 F1 Libra instrument. Hydroxyl radicals (˙OH) on the samples were identified by photoluminescence (PL) using terephthalic acid (TA) as a probe molecule under the UV irradiation. Electron spin resonance (ESR, JEOL, Japan) was used to detect ˙OH and superoxide anion radicals (˙O_2-) with 5,5-dimethylpyrroline-*N-o*xide (DMPO) as a spin-trap agent.

2.4. Photoelectrochemical measurements

The photoelectrochemical measurements were performed by a CHI 660B electrochemical analyzer (Chenhua, China) in a standard three-electrode system with a Pt counter electrode and a saturated calomel reference electrode. Mott-Schottky plots were determined in the range of -1.0 to 0.5 V (vs SCE) at a frequency of 1 kHz and 2 kHz in 0.2 M Na_2SO_4. A 125 W high-pressure mercury lamp (Philips) was used as a light source, and 0.5 M Na_2SO_4 aqueous solution was used as the electrolyte. The i–t curves were measured at 0 V bias potential.
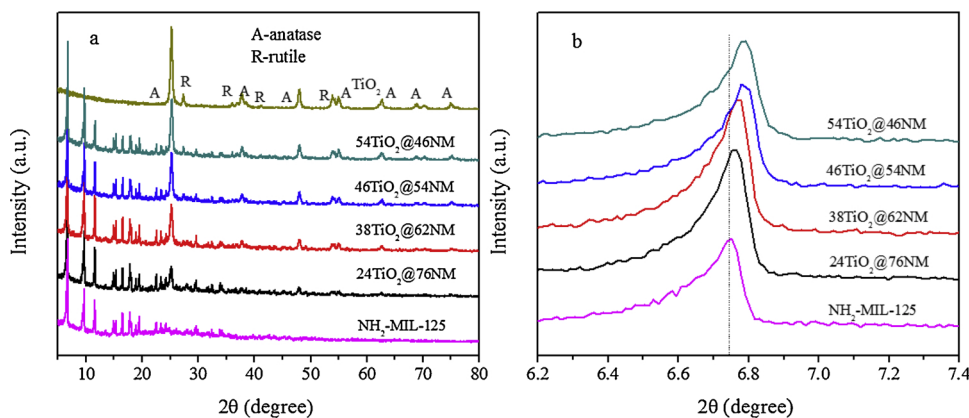
Fig. 1. XRD patterns (a) and enlarged view (b) of the TiO_2, NH_2-MIL-125 and $TiO_2@NH_2$-MIL-125 composites.

Electrochemical impedance spectroscopy (EIS) measurements were performed in the 0.5 M Na_2SO_4 aqueous solution over the frequency range of 0.1–100 kHz with the magnitude of 5 mV.

2.5. Evaluation of adsorption and photocatalytic activity

The adsorption and photocatalytic degradation measurements of HCHO were carried out in a home-made flow quartz reactor covered with a layer of aluminum foil on its inner wall in a continuous flow reactor maintained at 25 °C by water circulation (Fig. S1). A 125 W high-pressure mercury lamp (Philips) was used as a UV light source and the light intensity was 12 mW·cm^{-2} (UV at 365 nm as shown in Fig. S2), while a 300 W xenon lamp with a glass filter that cut off the light below 420 nm was used as visible light source and the light intensity was 150 mW·cm^{-2}. Two fans were fixed around the UV lamp to keep the flow system at room temperature. 0.1 g of catalyst was placed on a 250-mesh screen in the middle of the reactor for each experiment. The catalyst was placed in an oven at 120 °C for 3 h before each experiment. A 600 mL·min^{-1} air stream (20:80 vol% O_2:N_2) containing about 10 ppm of HCHO and water vapor (60% RH) was introduced into the reactor. The gaseous HCHO was produced by an air stream bubbling through HCHO solution. After the HCHO concentration had stabilized, the lamp was turned on, and the catalyst was exposed to the air stream containing the pollutant. The HCHO concentration was measured by an HCHO analyzer (Formaldemeter HTV-M, PPM Technology). The CO_2 and CO concentrations of inlet and outlet of the photoreactor were detected by a gas chromatography (GC).

To further investigate the adsorption capacity and the in-situ degradation of HCHO by the catalysts, the following batch experiments were carried out. Before the photocatalytic reaction, the catalyst was exposed to the HCHO-containing air stream in the dark until adsorption–desorption equilibrium was reached. Then the HCHO gas was stopped to inlet, and the UV light was turned on. The adsorption capacity and in-situ degradation properties of the samples were determined by detecting the HCHO concentration before and after the light was turned on. The in-situ degradation experiment was judged to have been completed when the HCHO concentration no longer changed under UV irradiation.

The removal efficiency and adsorption capacity of samples were calculated using the following formulas:

$$HCHO\ removal = (C_0 - C)/C_0 \tag{1}$$

$$HCHO\ adsorption\ capacity = \frac{F \cdot 1.226 \cdot 10^{-9}}{W}\left(C_0 t_s - \int_0^{t_s} C\ dt\right) \tag{2}$$

$$r = \frac{F \cdot 1.226 \cdot 10^{-9}}{60 \cdot W \cdot M_{HCHO}}(C_0 - C) \tag{3}$$

$$QE = \frac{(4 \times n_{co_2} + 2 \times n_{co}) \times N_A \times h \times c}{I \times S \times t \times \lambda} \times 100\% \tag{4}$$

where C_0 is the average HCHO concentration at the inlet under the stable steady (ppm). C is the corresponding value at the outlet at some time point (ppm), F is the total gas flow rate (mL·min^{-1}), W is the weight of the adsorbent (g), t is the adsorption time at some time point (min), and t_s is the adsorption saturation time (min). 1.226 is the conversion factor of ppm to mg·m^{-3} at the standard atmospheric pressure and 25 °C. r is the reaction rate (mol s$^{-1\,g-1}$), M_{HCHO} is the relative molecular mass of HCHO. QE is the quantum efficiency. n_{co_2} and n_{co} are the amount of CO_2 and CO molecules, respectively, N_A is Avogadro constant, h is the Planck constant, c is the speed of light, I is the intensity of irradiation light, S is the irradiation area, t is the photoreaction time, and λ is the wavelength of the light.

3. Results and discussion

3.1. Structural and morphological characterization

The amount of NH_2-MIL-125 in the $TiO_2@NH_2$-MIL-125 composites were calculated by TGA. The thermal analysis of TiO_2, NH_2-MIL-125 and $TiO_2@NH_2$-MIL-125 composites under N_2 atmosphere are shown in the TG curves in Fig. S3. For pure TiO_2, the TG curve showed a mass loss of only 1.05% upon heating to 600 °C. This loss can be attributed to the removal of water molecules in the sample. The addition of TiO_2 onto NH_2-MIL-125 can be confirmed by TG analysis. The mass loss at 120 °C was attributed to removal of adsorbed water molecules, desorbed organic ligand molecules and unremoved solvent molecules. A collapse of $TiO_2@NH_2$-MIL-125 composites occurred between 300 and 550 °C due to degradation of the carboxylic acid [28]. The TG curve of NH_2-MIL-125 is similar to that of $TiO_2@NH_2$-MIL-125 composites. It is calculated from the TG curve in the range up to 600 °C that the content of TiO_2 in $TiO_2@NH_2$-MIL-125 ranged from 24 wt% to 54 wt%.

The crystal structure and phase of TiO_2, NH_2-MIL-125 and $TiO_2@$ NH_2-MIL-125 were analyzed by XRD. As shown in Fig. 1a, all the samples showed high crystallinity. The XRD of the pure NH_2-MIL-125 was comparable to results previously reported in the literature [23,29], indicating that the NH_2-MIL-125 was successfully synthesized. Both
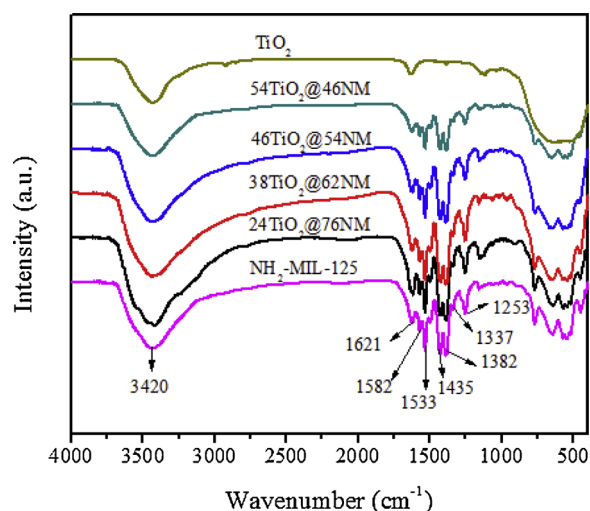
Fig. 2. FT-IR spectra of TiO_2, NH_2-MIL-125 and the TiO_2@NH_2-MIL-125 composites.

anatase (JCPDS 21-1272) and rutile (JCPDS 21-1276) types of TiO_2 were identified in TiO_2@NH_2-MIL-125 during the nucleation and growth of the MOF. The diffraction peaks of both NH_2-MIL-125 and TiO_2 were detected in TiO_2@NH_2-MIL-125, which indicated the presence of both solids. In addition, the characteristic diffraction peaks of TiO_2 were enhanced due to the increase content of TiO_2. Fig. 1b shows that the main peak of TiO_2@NH_2-MIL-125 shifts to a large-angle side, which may be due to the strong interaction between TiO_2 and NH_2-MIL-125 in the composites formed during the self-assembly process. The crystallite size were calculated from the Scherrer equation are shown in Table S1. We can see that the crystallite size of different samples did not change significantly and minor variation was within the calculation error range. This is because that the conditions for preparing the samples do not change the crystallite size of TiO_2. From the TEM images of 46TiO_2@54NM, the particle size of TiO_2 was about 20 nm, which was in good agreement with the crystallite size by calculating the Scherer equation. We also analyzed the anatase/rutile ratio. Based on the respective peak intensities, the weight fraction of the rutile phase in the TiO_2 can be calculated from $x = (1 + 0.8I_A/I_R)^{-1}$ where x is the weight fraction of the rutile phase, and I_A and I_R are the intensities of anatase and rutile peaks, respectively [30]. The results showed that the pure TiO_2 contains 84.6% of anatase and 15.4% of rutile. In addition, the content of TiO_2 anatase increased with the increase of NH_2-MIL-125 content. This indicated that NH_2-MIL-125 may inhibit the transformation of TiO_2 from anatase to rutile phase.

In order to further clarify the functional groups and molecular structure of the samples, the FT-IR spectra of the TiO_2@NH_2-MIL-125 composites were measured, and the results are shown in Fig. 2. The spectra of the TiO_2@NH_2-MIL-125 composites are similar to the pure NH_2-MIL-125, indicating that TiO_2 did not hinder the formation of the NH_2-MIL-125. The broad band at 3420 cm^{-1} is due to the free solvent molecules trapped within the pores or the hydroxyl stretching vibration associated with adsorbed water [17,31]. The bands at 1253 and 1337 cm^{-1} are attributed to the C–N stretching vibration [29–32]. The bending vibration of C=O of aromatic amines can be seen at 1621 cm^{-1} [26]. The distinct peaks at 1435 and 1533 cm^{-1} are signed to the asymmetric vibrations of carboxylate linker and the 1382 and 1582 cm^{-1} are due to symmetric vibrations [30–33]. Bands in the 400¯800 cm^{-1} region (at 774, 644 and 451 cm^{-1} for the composites) is associated with a characteristic vibration peak of [TiO_6] ligand and matches the

stretching vibration peak of O−Ti−O [34]. These findings further show that the structure of the NH_2-MIL-125 was retained during the self-assembly process. The wavenumber of C=O shifted from 1621 cm^{-1} at NH_2-MIL-125 to 1645 cm^{-1} at 46TiO_2@54NM, suggesting the presence of interactions between two components of the nanocomposites [26].

XPS spectra measurements were carried out to clarify the surface chemical states of the samples. The wide-scan XPS spectra of Fig. 3a shows that there are obvious peaks of C 1s, N 1s, O 1s and Ti 2p in the 46TiO_2@54NM and NH_2-MIL-125 samples. The results of the high-resolution XPS spectra of C 1s, N 1s, O 1s and Ti 2p in the three samples are shown in Fig. 3b-3e. As in the case of the pure NH_2-MIL-125, the C 1s peak at 284.8 eV was used as a reference from adventitious carbon. The peaks at 286, 286.58, 288.78 eV correspond to the C–N, CC and CO−= bonds, respectively (Fig. 3b). Fig. 3c shows the N 1s spectrum of pure NH_2-MIL-125 and can be deconvoluted into three peaks. The peaks at 399.34 and 402.3 eV can be assigned to -NH_2 and graphitiC–N species (-NH-$^+$), respectively, and the peak at around 399.9 eV can be related to the residual DMF (N−CO=) in the framework [35,36]. In Fig. 3d, the peaks of Ti $2p_{3/2}$ and Ti $2p_{1/2}$ in pure NH_2-MIL-125 at 458.9 and 464.7 eV, respectively, indicate that the oxygen bounded titanium remains in the oxidation state of Ti^{4+} species in the Ti−O cluster [37,38]. The O 1s XPS spectrum of NH_2-MIL-125 can be divided into three peaks. The peak at 532.55 eV is assigned to OH groups. The peaks at 530.38 and 531.82 eV correspond to Ti−O and C=O, respectively [39]. Compared with the pure NH_2-MIL-125, the C 1s, N 1s, Ti 2p and O 1s XPS peaks of 46TiO_2@54NM are shifted slightly to lower binding energies. This observation can be attributed to the stronger electronic interaction (*Ti−N-C*) between *Ti*−OH on the surface of TiO_2 and C−NH_2 groups of NH_2-MIL-125 [40,41]. Note that this analysis of the XPS analysis can also explain the shift of the XRD due to the formation of Ti−N−C bonds. In Fig. 3d, the Ti 2p XPS peaks of 46TiO_2@54NM before and after 122 h of photocatalytic reaction have no obvious change and shift, indicating that the catalyst has an excellent stability. In addition, the surface atomic percentage on 46TiO_2@54NM did not change significantly before and after 122 h of photocatalytic reaction as shown in Table S2.

The Raman spectroscopy was also carried out to detect the interaction between NH_2-MIL-125 and TiO_2. As shown in Fig. 4, the main vibration bands at 142 cm^{-1} (E_g), 395 cm^{-1} (B_{1g}), 515 cm^{-1} (A_{1g}) and 637 cm^{-1} (E_g) correspond to the anatase phase of TiO_2. And the vibration mode at 824 cm^{-1} (B_{2g}) is attributed to the rutile TiO_2. It is worth noting that the E_g (142 cm^{-1}) mode in 46TiO_2@54NM is slightly red-shifted compared with pure TiO_2. The red-shift of the E_g can be attributed to the covalent bonds that link NH_2-MIL-125 and TiO_2 in the 46TiO_2@54NM composite.

The morphologies of the catalysts were analyzed by SEM images. As shown in Fig. 5a, the pure NH_2-MIL-125 was composed of flat circular grains with an average size of about 1 μm. Fig. 5f shows the SEM images of TiO_2 with a mean size of 25 nm and aggregated nanoparticles were observed. Such agglomeration can be well avoided by introducing NH_2-MIL-125 into the TiO_2@NH_2-MIL-125 composites. In Fig. 5b-e, highly dispersed grains of TiO_2 on the surface of NH_2-MIL-125 can be seen, which promotes the contact between the target contaminant and the catalyst in the catalytic process. However, obvious aggregation of TiO_2 was observed in 54TiO_2@46NM compared with 46TiO_2@54NM, which is not conducive to the progress of the photocatalytic reaction. It is the intimate contact between NH_2-MIL-125 and TiO_2 that facilitates electron transfer between the two semiconductors. Fig. 6 shows the HR-TEM images of 46TiO_2@54NM. It can be clearly observed that TiO_2 are intimately adhering on the edges of NH_2-MIL-125. Additionally, the clearly interface between TiO_2 and NH_2-MIL-125 was formed during the self-assembly process. It is important for the interface charge
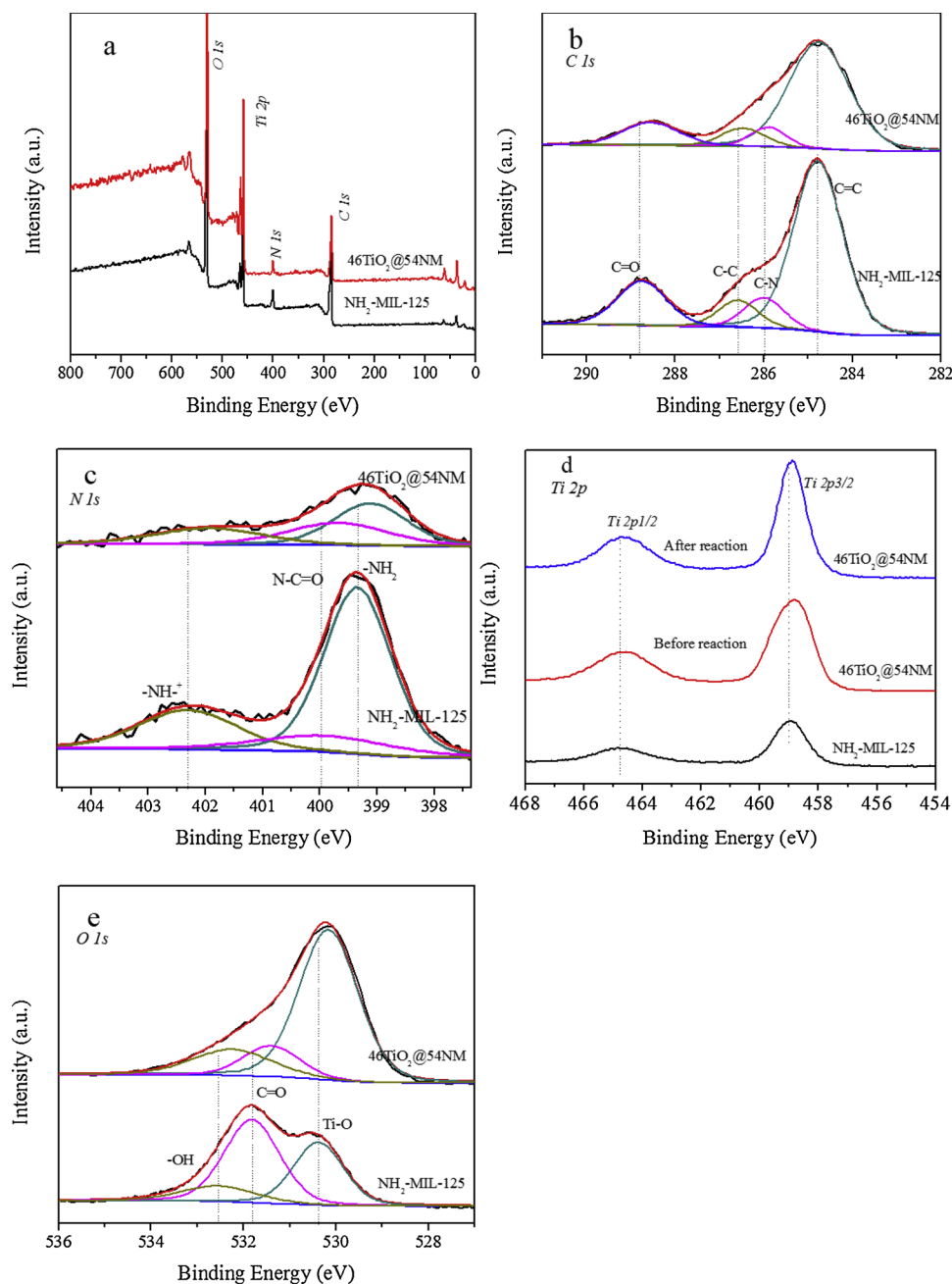
Fig. 3. XPS spectra of the NH$_2$-MIL-125 and 46TiO$_2$@54NM composite in the: survey (a), C 1s (b), N 1s (c), Ti 2p (d), O 1s (e).

transfer between TiO$_2$ and NH$_2$-MIL-125, which is beneficial to improve the photocatalytic activity of samples. The EDS spectrum confirmed the presence of C, N, Ti and O elements in the composite.

The specific surface area, total pore volume and pore size distribution in the samples were analyzed by N$_2$ adsorption-desorption, and the results are shown in Fig. 7 and Table 1. The pure NH$_2$-MIL-125 exhibits type I sorption isotherms, suggesting that it is a typical microporous structure with narrow pore diameter of about 0.8 nm as determined by the Horvath-Kawazoe method [28,42]. However, a very small hysteresis loop can be observed in the diagram (P/P$_0$, 0.5~1.0), and its formation is related to the capillary condensation, which indicates that there is also a certain meso/macroporous structure in the

NH$_2$-MIL-125 by the Barrett-Joyner-Halenda method. The presence of the mesoporous structure can be clearly observed in Fig. 7c. In the photocatalytic process, the presence of a certain amount of mesoporous structure facilitates the rapid diffusion of gas molecules from the pores, improving the efficiency of the photocatalytic reaction. The pure TiO$_2$ have a type IV isotherm, indicating the presence of mesopores (2–50 nm). Moreover, the hysteresis loop of pure TiO$_2$ is H3 type in the higher relative pressure range (P/P$_0$, 0.8~1.0), which means that there are slit-like pores and capillary agglomeration in the mesopores [2,28]. 46TiO$_2$@54NM exhibited mixed I/IV type isotherms with a large hysteresis loop, indicating the presence of micropores and mesopores. The specific surface area and pore volume of NH$_2$-MIL-125 are 1301 m^3/g
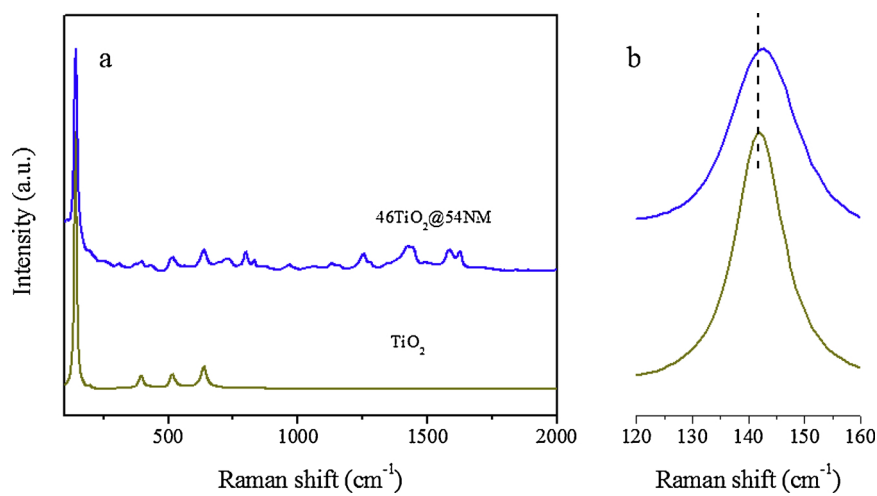
Fig. 4. Raman spectra (a) and enlarged view (b) of TiO$_2$ and 46TiO$_2$@54NM.
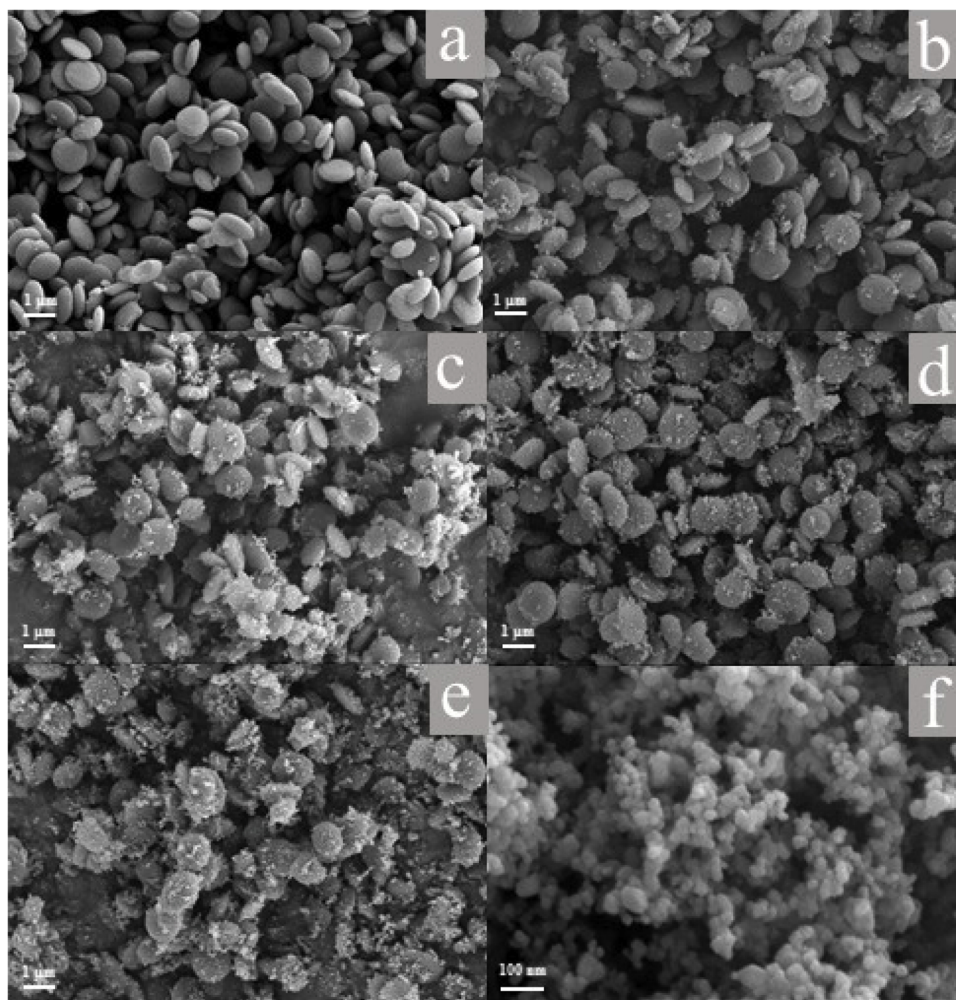
Fig. 5. SEM images of the NH$_2$-MIL-125 (a), 24TiO$_2$@76NM (b), 38TiO$_2$@62NM (c), 46TiO$_2$@54NM (d), 54TiO$_2$@46NM (e) and TiO$_2$ (f).
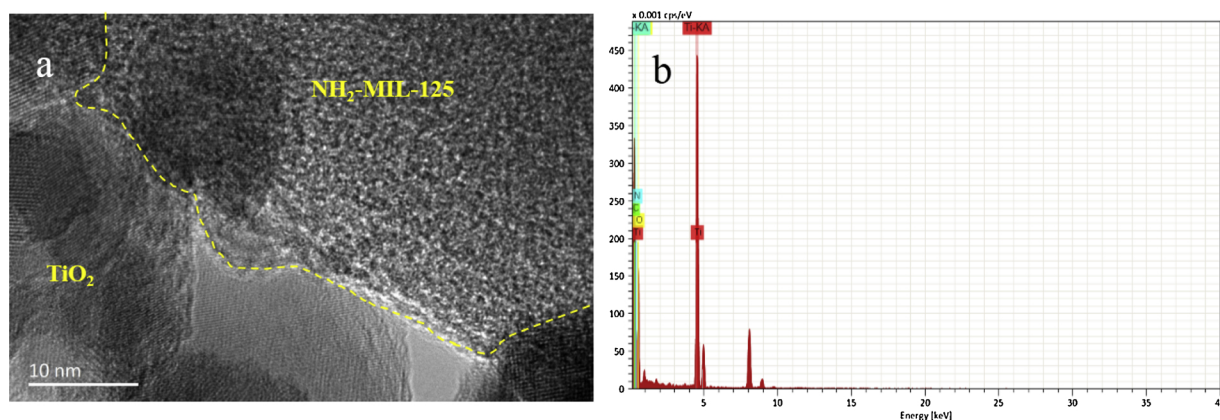
Fig. 6. HR-TEM images (a) and EDS (b) of $46TiO_2@54NM$.

and $0.638\ cm^3/g$, respectively. The corresponding values of TiO_2 are $56\ m^3/g$ and $0.22\ cm^3/g$, respectively. The specific surface area and pore volume of the $46TiO_2@54NM$ lie between the values for the two pure substances, with the corresponding values of $789\ m^3/g$ and $0.412\ cm^3/g$ (Table 1), respectively. The NH_2-MIL-125 and $46TiO_2@54NM$ exhibit a higher fraction of micropores. In general, larger specific surface area and smaller pore size in catalysts are associated with more adsorption sites and catalytic sites for the removal of the target pollutant, in this case, formaldehyde.

The UV–vis diffuse reflectance spectra of the samples are shown in Fig. 8a. After in-situ recombination of TiO_2 with NH_2-MIL-125, the absorption spectra of the composites are very close to that of NH_2-MIL-125 and gradually red-shifted as the NH_2-MIL-125 content increased.

And from the Fig. S4, the maximum absorption of the composites were about 470 nm. This phenomenon may be ascribed to a close binding (Ti-N-C) between TiO_2 and NH_2-MIL-125, which can facilitate the generation of more electrons-hole to effectively remove contaminants. The band-gaps energy (E_g) of samples can be evaluated using the tangents of $(ahv)^n$ *vs.* photo energy. As shown in Fig. 8b and c, the band gaps (E_g) of pure TiO_2 and NH_2-MIL-125 are estimated to be about 3.1 and 2.47 eV, respectively. Fig. 9 shows the typical Mott-Schottky plot of pure NH_2-MIL-125 at a frequency of 1 and 2 kHz. The result reveals that NH_2-MIL-125 is a typical *n*-type semiconductor, and the flat band potential of pure NH_2-MIL-125 is 1.07 V vs SCE (equivalent to 0.82 V vs. NHE). It is known that the flat band potential of an *n*-type semiconductor is equal to its Fermi level, and the conduction band of such an *n*-type
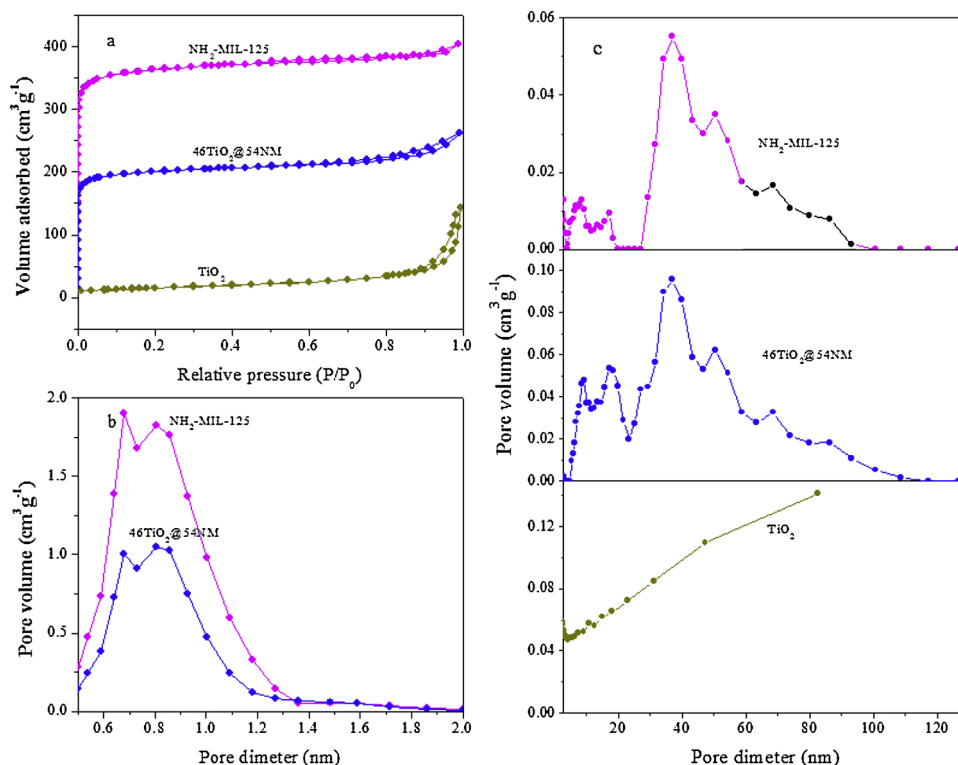

Fig. 7. Nitrogen adsorption-desorption isotherms (a) and pore size distribution curves (b, c) of the TiO_2, NH_2-MIL-125 and $46TiO_2@54NM$ composite.

Table 1
Structural parameters and adsorption capacity of the samples.

samples	BET surface area (m²/g)	t-Plot micropore area (m²/g)	average pore size (nm)	pore volume (cm³/g)	adsorption capacity (mg/g)
NH₂-MIL-125	1301	1147	1.93	0.638	31.8
46TiO₂@54NM	789	679	2.08	0.412	18.5
TiO₂	56	–	15.89	0.220	0.434

semiconductor is more negative than the flat band potential by about 0.10 V [43]. Thus the conduction band (CB) of pure NH₂-MIL-125 can be estimated to be -0.72 V vs. NHE. The valence band (VB) of pure NH₂-MIL-125 can be calculated using the formulas: $E_{CB} = E_{VB} - E_g$, so the VB of pure NH₂-MIL-125 is +1.75 V vs. NHE.

3.2. Photocatalytic activities

The photocatalytic activities of the samples were evaluated through photo-oxidation of HCHO gas under UV irradiation in the continuous flow reactor and the RH was set at 60% (Fig. S5). To test the possible photolysis of HCHO in the photoreactor, the removal rate of HCHO was also detected under UV light irradiation without photocatalyst. The experimental results showed that HCHO itself could not be removed under UV light irradiation (Fig. S6). As shown in Fig. 10a, only 15% of HCHO removal efficiency was obtained on pure NH₂-MIL-125, indicating that NH₂-MIL-125 itself has low activity for the photocatalytic HCHO degradation. And the HCHO removal efficiency was 70% over the pure TiO₂. The TiO₂@NH₂-MIL-125 composite showed a significant improvement of HCHO removal comparing to the pure NH₂-MIL-125 and TiO₂, which was probably because of the efficient interfacial charge transfer between TiO₂ and NH₂-MIL-125 in the composite. When the TiO₂ content increased from 24 wt% to 46 wt%, the activity of TiO₂@NH₂-MIL-125 gradually increased from 73% to 90%. However, when
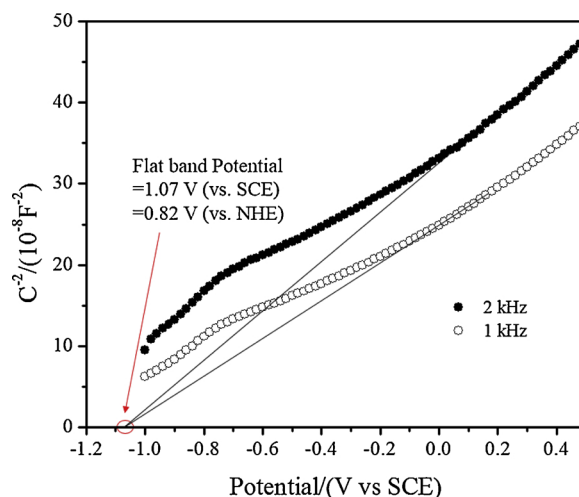
Fig. 9. Mott-Schottky plot of NH₂-MIL-125 in a 0.2 M Na₂SO₄ aqueous solution.

the TiO₂ content further increased to 54 wt%, the HCHO removal decreased to 78%. This observation was probably a result of excess TiO₂ not only reducing the interfacial contact between TiO₂ and NH₂-MIL-125 but also increasing the recombination of the photoinduced charges,
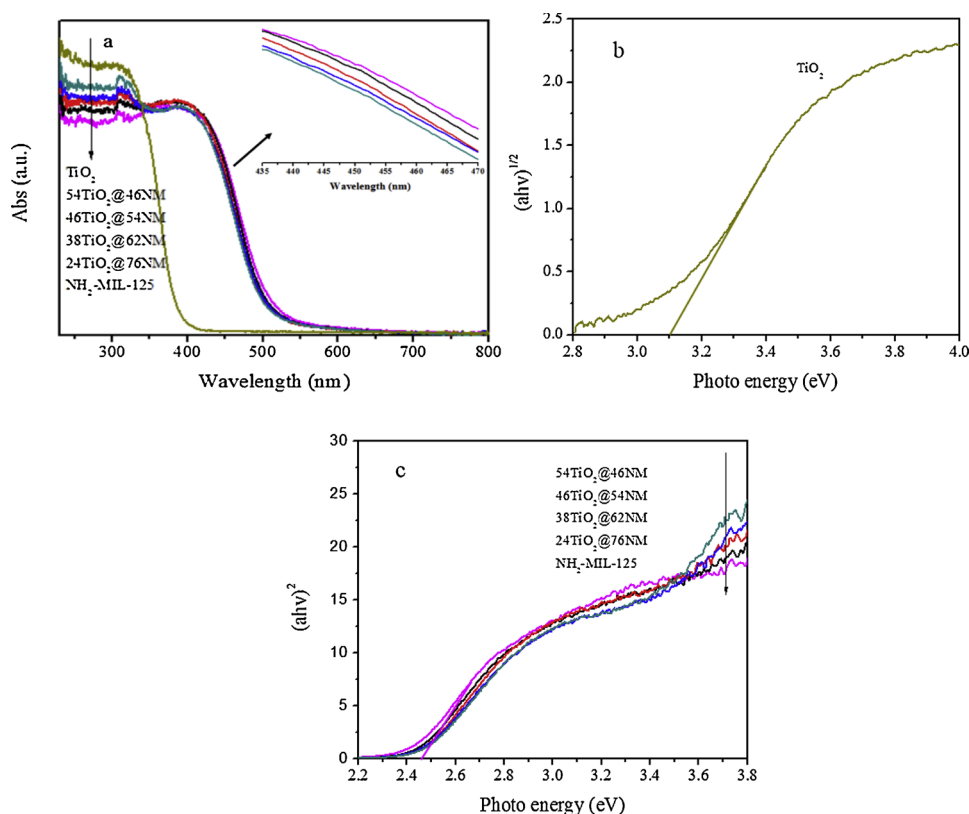

Fig. 8. UV–vis diffuse reflectance spectra (a), Plots of $(\alpha h\nu)^{1/2}$ against photon energy (b) of TiO₂, Plots of $(\alpha h\nu)^2$ against photon energy (c) of NH₂-MIL-125 and TiO₂@NH₂-MIL-125.
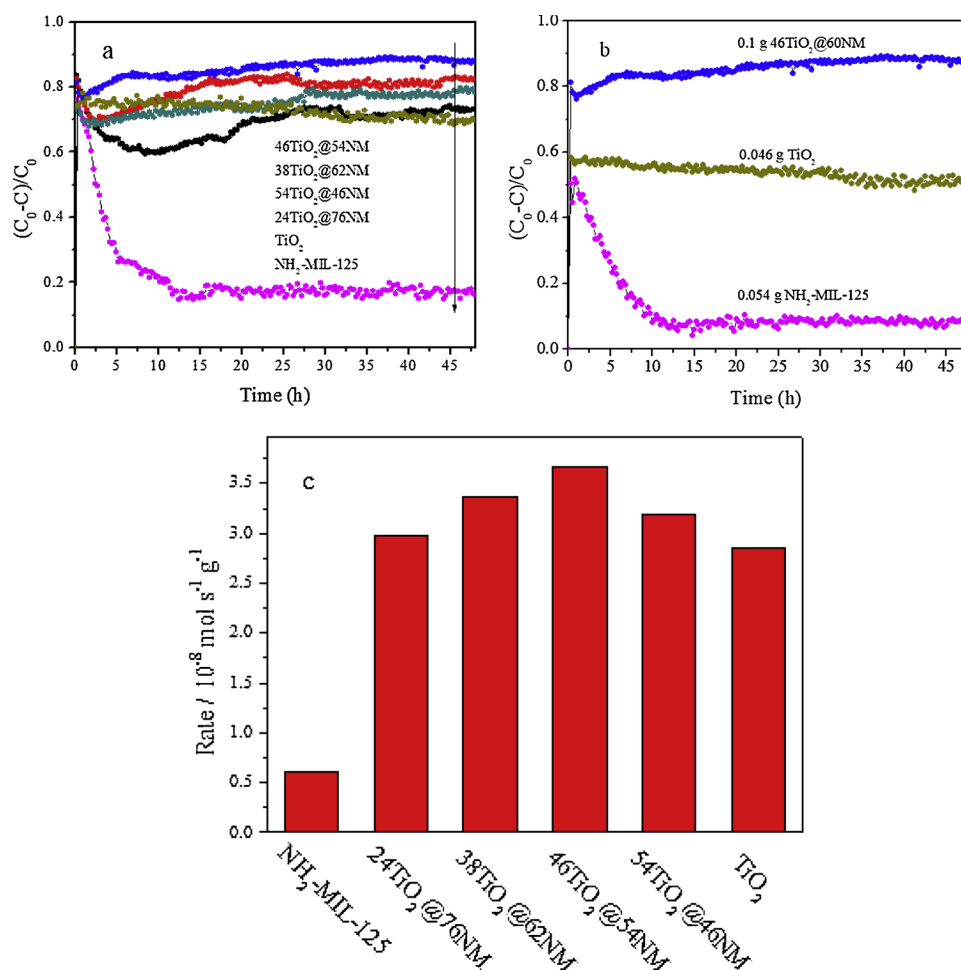
Fig. 10. Photocatalytic activities of different samples under UV light. TiO_2, NH_2-MIL-125 and composites with different TiO_2/NM ratios (a), the composite and single components (b), and reaction rate of different samples (c).
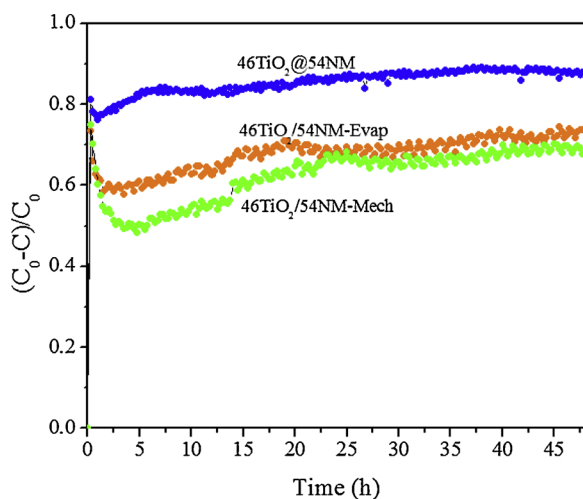

Fig. 11. Photocatalytic activities of 46TiO_2@54NM, 46TiO_2/54NM-Mech and 46TiO_2/54NM-Evap under UV.

resulting in lower photocatalytic activity. Therefore, the combination TiO_2 with NH_2-MIL-125 in an appropriate ratio through covalent bond is important to improve the removal efficiency of HCHO. In addition, in the beginning stage of the photocatalytic reaction with all the composites, the degradation curve of HCHO showed a concave shape, which may be due to the high adsorption capacity of NH_2-MIL-125. The reaction rates of different samples are presented in Fig. 10c. The reaction rate of samples increased first and then decreased with the increase in the TiO_2 content. When the content of TiO_2 was 46 wt%, the reaction rate reached a maximum. The value of 46TiO_2@54NM (3.67·10^{-8} mol $s^{-1} g^{-1}$) was 6 times and 1.3 times higher than that of NH_2-MIL-125 (0.61·10^{-8} mol $s^{-1} g^{-1}$) and TiO_2 (2.86·10^{-8} mol $s^{-1} g^{-1}$), respectively. This is due to a synergistic effect between the two semiconductors [44–46]. Moreover, the concentration changes of CO_2 and CO during the HCHO degradation were discussed and shown in Fig. S7. The CO_2 concentration remained around 9 ppm, while the CO concentration almost unchanged, implying a completely decomposition of HCHO into CO_2 and H_2O under UV irradiation in the continuous flow reactor. However, at the first 15 min of the photocatalytic reaction, the increase of CO_2 concentration was significantly higher than the decrease of HCHO concentration, which was mainly attributed to desorption of
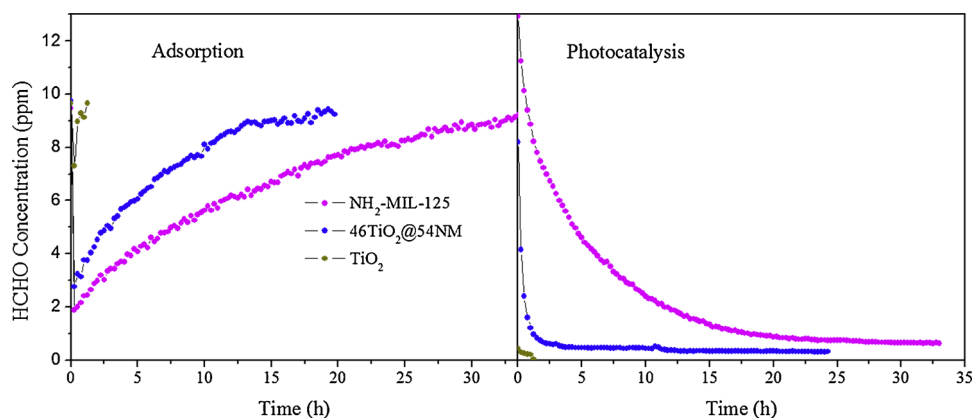
Fig. 12. Adsorption breakthrough and in-situ degradation curve of HCHO for NH_2-MIL-125, $46TiO_2@54$ N and TiO_2.

HCHO from the reactor surface, and the subsequent oxidation to CO_2, as well as measurement error of CO_2 [47–49]. As for TiO_2, the CO_2 concentration gradually decreased as the reaction time prolonged, and the CO concentration did not change significantly at around 1 ppm. Therefore, the composite catalysts showed a higher CO_2 selectivity and stability than TiO_2. Furthermore, the quantum efficiency of $46TiO_2@54NM$ and TiO_2 were calculated to be 0.711% and 0.44%, respectively. This indicated that $46TiO_2@54NM$ is a more efficient photocatalyst than the pure TiO_2. In contrast, under visible light the HCHO removal rate for $64TiO_2@54NM$ at 4 h was almost zero (Fig. S8), indicating that $46TiO_2@54NM$ has a low activity for the photocatalytic HCHO degradation under visible light irradiation, probably because the photocatalytic activity of NH_2-MIL-125 is low. Therefore, the UV light was applied to the whole experiments.

Fig. 10b shows the photocatalytic activities of the composite and single components under UV light irradiation. The photocatalytic degradation of HCHO by $46TiO_2@54NM$ was significantly higher than the sum of TiO_2 (HCHO removal) and NH_2-MIL-125 (8% HCHO removal). Furthermore, the HCHO removal efficiency remained at 90% after 48 h of UV irradiation. In contrast, the photocatalytic activity of TiO_2 decreased over time, with HCHO removal decreasing from 58% to 49% after 48 h of photoreaction. It can be seen from the SEM images that the
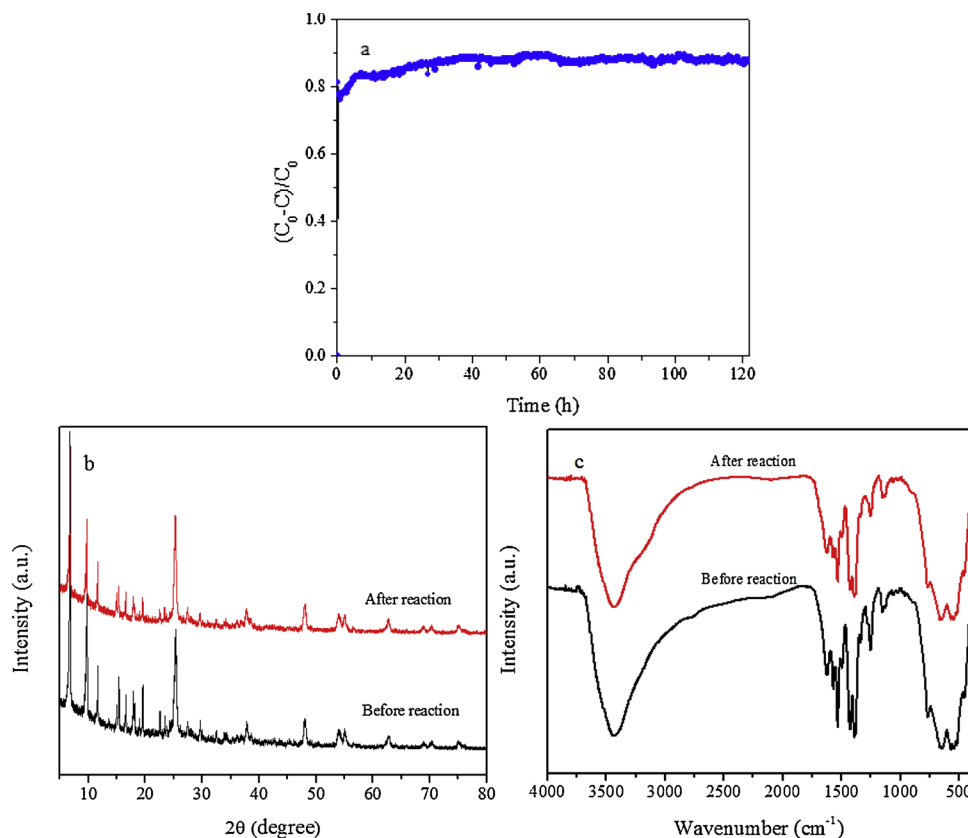

Fig. 13. Photocatalytic activity (a), the XRD patterns (b) and FT-IR spectra (c) of $46TiO_2@54NM$ before and after the photocatalytic reactions.
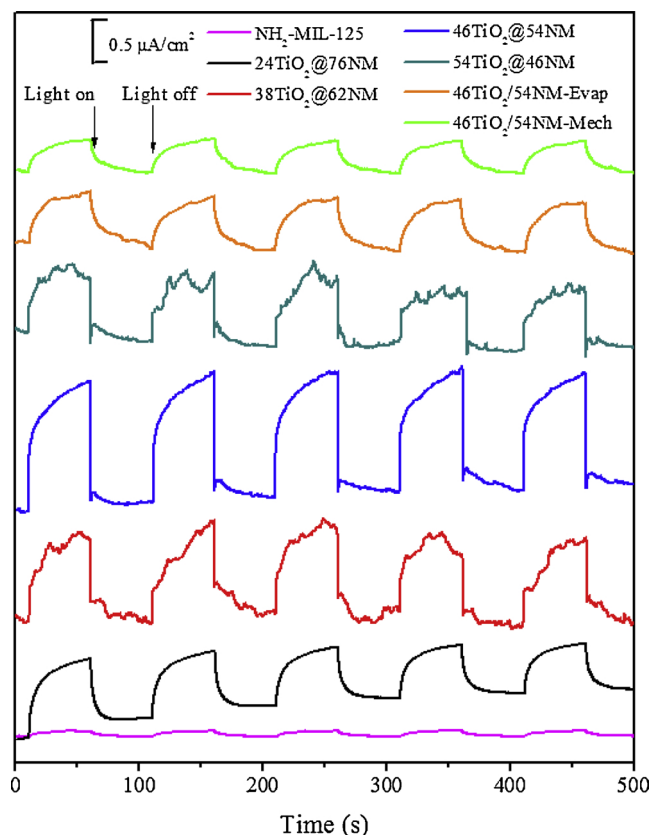
Fig. 14. Photocurrent transient response of different catalysts.

morphology of the 46TiO$_2$@54NM did not change significantly during the reaction, in contrast to the pure TiO$_2$ which showed an obvious agglomeration and a change of morphology over this time (Fig. S9). These data indicate that the composite catalyst is quite stable over the course of the photocatalytic oxidation of HCHO.

To explore the importance of intimate junctions for composite catalysts, we compared the activity of 46TiO$_2$@54NM composite with that of 46TiO$_2$@54NM-Mech and 46TiO$_2$/54NM-Evap under UV light. The results showed that the order of decreasing photocatalytic activity was 46TiO$_2$@54NM > 46TiO$_2$/54NM-Evap > 46TiO$_2$/54NM-Mech (Fig. 11); that is, the 46TiO$_2$@54NM composite synthesized by an in-situ solvothermal method showed a higher activity than the composites prepared by mechanical mixing and solvent evaporation methods. This behavior may be attributed to the closer connection between NH$_2$-MIL-125 and TiO$_2$ in the self-assembled composite, which is favorable to the charge transfer, thereby improving the photocatalytic activity of the composite.

The adsorption capacity and the degradation efficiencies of the catalysts for HCHO were also investigated. As shown in Fig. 12, Table 1 and Table S3, the adsorption breakthrough time of 46TiO$_2$@54NM was reached at 18.5 h, the adsorption capacity was calculated to be 18.5 mg/g, and the adsorbed HCHO could be degraded efficiently under UV irradiation only for 4 h. The pure NH$_2$-MIL-125 exhibited a higher HCHO saturation uptake of 31.8 mg/g and a longer breakthrough time of 33.5 h, but it took a long time (about 32 h) to remove most of the adsorbed HCHO. This was due to the lower photocatalytic activity of NH$_2$-MIL-125. Significantly, the adsorption capacity of NH$_2$-MIL-125 was much higher than that of MIL-125 (0.72 mg/g, Fig. S10), indicating that the NH$_2$ groups is the main adsorption sites for HCHO. TiO$_2$ has the

lowest HCHO adsorption uptake at 0.434 mg/g, so the amount of photocatalytic removal of HCHO with this material was small. Therefore, it can be seen that the composite catalysts exhibited a synergistic effect between the adsorption and photocatalytic oxidation properties. Table S3 summarized the existing research results, the NH$_2$-MIL-125 has the advantages as an excellent adsorbent on adsorption capacity and breakthrough time for HCHO removal.

The excellent performance of TiO$_2$@NH$_2$-MIL-125 in HCHO removal can be explained by the characterization analyses above. From the FT-IR spectra (Fig. 2), N$_2$ adsorption-desorption isotherms and pore size distribution curves (Fig. 7) of the samples, NH$_2$-MIL-125 has abundant surface -NH$_2$ and −OH functional groups, as well as large specific surface area, pore volume and microporous structure, which offer more adsorption sites for HCHO. From the XPS spectra Raman spectra of the samples (Fig. 3 and 4), we know that Ti-*N-C* covalent bonds were formed in TiO$_2$@NH$_2$-MIL-125, which is more favorable for charge transfer between TiO$_2$ and NH$_2$-MIL-125. The different preparation methods of the TiO$_2$@NH$_2$-MIL-125 further illustrate the importance of the close contact between the two semiconductors for improving the HCHO removal rate due to a more efficient charge transfer. In addition, the open pore structure not only facilitates contact between HCHO and the active sites, but it also improves mass transfer within the material structure during photocatalytic process. In short, TiO$_2$@NH$_2$-MIL-125 exhibited excellent HCHO removal as a result of the synergistic effect between adsorption of HCHO on NH$_2$-MIL-125 and efficient interfacial charge transfer between the two phases of the composite catalyst.

In order to evaluate the stability of the material, the photocatalytic oxidation was carried out for an extended period of time. As shown in Fig. 13a, after 122 h of photocatalytic reaction, the HCHO removal rate over 46TiO$_2$@54NM remained at 90% without a significant decay. In order to evaluate the stability of the structure, the crystal structure and phase of 46TiO$_2$@54NM before and after 122 h of continuously photocatalytic reaction was tested by XRD (Fig. 13b). No extra diffraction peaks were observed in XRD pattern, which indicated that the positions and intensities of the peaks were nearly the same. This also indicated that no crystalline structure changes after the photocatalytic reaction. The FT-IR spectra also showed that no obvious change was observed after the 122 h of photocatalytic reaction (Fig. 13c). In addition, the amount of NH$_2$-MIL-125 in the used 46TiO$_2$@54NM was calculated by TGA (Fig. S11). The calculated results showed that the content of TiO$_2$ in the used 46TiO$_2$@54NM was 48% (46% TiO$_2$ in the fresh 46TiO$_2$@54NM), indicating that the material has an excellent stability.

3.3. Proposed photocatalytic pathway

The interface charge transfer behavior was investigated in the electrochemical experiment (Fig. 14 and Fig. S12). The photocurrent response was measured for the different catalysts under on-off cyclical UV light. TiO$_2$@NH$_2$-MIL-125 had higher photocurrent response than did NH$_2$-MIL-125, showing that the former had a lower recombination of photogenerated carriers than the latter. In addition, 46TiO$_2$@54NM showed a higher photocurrent response than 46TiO$_2$/54NM-Mech and 46TiO$_2$/54NM-Evap, which was attributed to a stronger electronic interaction (Ti-*N-C*) between NH$_2$-MIL-125 and TiO$_2$ by in-situ self-assembled method than the mechanical mixing and solvent evaporation methods. This observation confirmed the importance of the effective combination between the two phases of the composite catalyst. Consistent with the results of the photocurrent response, the EIS of 46TiO$_2$@54NM exhibits a smaller arc radius than other catalysts (Fig. S12), indicating the smallest charge transfer resistance in 46TiO$_2$@54NM. This may be because the tighter interfacial contact of TiO$_2$ and
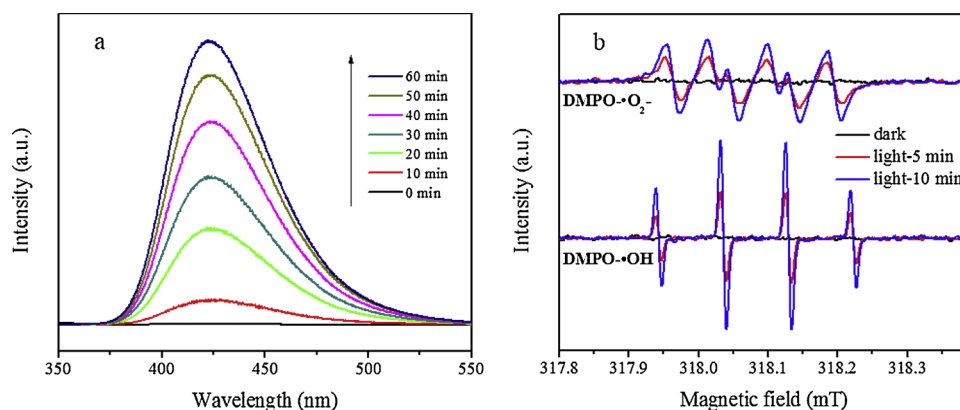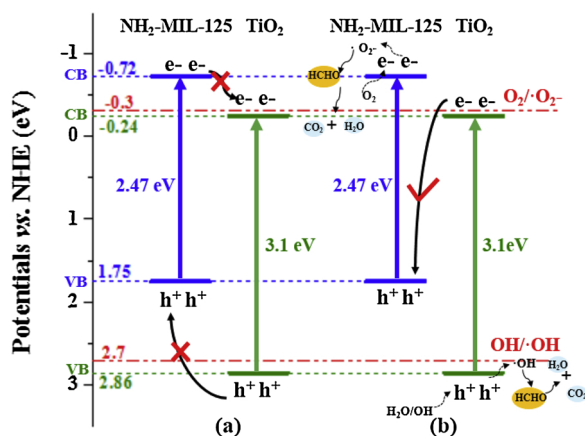
Fig. 15. PL spectral changes detected in the presence of $2 \cdot 10^{-3}$ M NaOH solution with $5 \cdot 10^{-4}$ M terephthalic acid (a) and ESR spectra of $\cdot OH$ and O_2^- radicals (b) over 46TiO$_2$@54NM under UV light.

Scheme 1. Proposed photocatalytic reaction mechanisms of the TiO$_2$@NH$_2$-MIL-125 composite under UV irradiation. (a) conventional heterojunction-type and (b) Z-scheme mechanisms.

MOF provides a more efficient electron transfer pathway than charge accumulation [50].

In order to provide clues to understand the mechanism accounting for the enhanced photocatalytic activity of 46TiO$_2$@54NM, $\cdot OH$ radicals on the surface of 46TiO$_2$@54NM were measured by PL spectra using TA as a probe molecule. As shown in Fig. 15a, a broad peak was observed around 425 nm in a $2 \cdot 10^{-3}$ M NaOH solution with $5 \cdot 10^{-4}$ M TA (excited at 315 nm). This peak was attributed to TA$-$OH, which was produced by the reaction of $\cdot OH$ radicals with TA [2]. The peak intensity increased gradually with increasing irradiation time, indicating that the $\cdot OH$ radicals were generated. In addition, ESR measurement was used to detect $\cdot OH$ and $\cdot O_2$- radicals over the 46TiO$_2$@54NM composite under UV irradiation. As shown in Fig. 15b, six characteristic peaks of DMPO-$\cdot O_2$- can be found after the light irradiation [50]. The intensity ratio of 1:2:2:1 can be classified as the characteristic peaks of DMPO-$\cdot OH$ [51]. The peak intensities increased with the irradiation time. Consequently, it can be concluded that the $\cdot OH$ and $\cdot O_2$- radicals play important roles in the photocatalytic degradation of HCHO.

Based on the above experimental results and characterization analyses, we propose a possible mechanism for the enhanced photocatalytic degradation of HCHO over TiO$_2$@NH$_2$-MIL-125 nanocomposites. As shown in Scheme 1, the CB/VB of TiO$_2$ has been reported to be -0.24/2.86 eV. The CB/VB of NH$_2$-MIL-125 are about -0.72 /1.75 eV. Considering the VB/CB of TiO$_2$ and NH$_2$-MIL-125 and the standard

redox potential of OH-/$\cdot OH$ (2.7 V *vs.* NHE) and O$_2$/$\cdot O_2^-$ (-0.3 V *vs.* NHE) couples, respectively, only photogenerated holes from the VB of TiO$_2$ can react with water molecules or surface hydroxyls to generate $\cdot OH$ radicals. Similarly, only electrons from the CB of NH$_2$-MIL-125 can react with adsorbed O$_2$ molecules to produce $\cdot O_2$- radicals. If the 46TiO$_2$@54NM follows the conventional heterojunction-type mechanism (Scheme 1a), which is not favorable for the formation of $\cdot OH$ and $\cdot O_2^-$ radicals, it could result in a lower photocatalytic activity. Thus, a Z-scheme is more reasonable for the photocatalytic oxidation of HCHO on the composite (Scheme 1b). Under UV light irradiation, both TiO$_2$ and NH$_2$-MIL-125 are directly excited and generated electrons and holes, and electrons are excited from the valence band to conduction band. The photogenerated holes remain at the VB of TiO$_2$, and the photoexcited electrons are transferred to the VB of NH$_2$-MIL-125 through the interaction between TiO$_2$ and NH$_2$-MIL-125. This facilitates the separation of the photogenerated carriers. Electrons stored in the CB of NH$_2$-MIL-125 can react with adsorbed molecular oxygen on the surface of NH$_2$-MIL-125 to generate $\cdot O_2^-$ radicals, and holes stored in the VB of TiO$_2$ can react with water molecules or surface hydroxyls near the surface of TiO$_2$ to form $\cdot OH$ radicals. These reactive oxygen species can oxidize HCHO to produce H$_2$O and CO$_2$.

4. Conclusions

In summary, TiO$_2$@NH$_2$-MIL-125 nanocomposites were synthesized using a simple in-situ solvothermal method and for the first time by using TiCl$_4$ as titanium source of MOFs. The composite samples possessed large specific surface area and pore volume, microporous structure (including mesoporous structure), which promote the dispersion of TiO$_2$, offer more adsorption sites and facilitate mass transfer. Overall, TiO$_2$@NH$_2$-MIL-125 showed much higher photocatalytic activity than pure NH$_2$-MIL-125 and TiO$_2$, which were ascribed to the compact connection between the two phases that can facilitate interfacial charge transfer. The high HCHO adsorption capacity can shorten traveling distance between HCHO on the adsorption sites and catalytic active sites, thereby further improving the photocatalytic activity. The results of this work highlight the synergistic effect between semiconductors and MOFs nanocomposites as a high-performance catalyst, thereby encouraging additional work in the exploration and research of MOFs in the field of environmental pollution control.

Declaration of Competing Interest

The authors declare that they have no known competing financial

interests or personal relationships that could have appeared to influence the work reported in this paper.

Acknowledgments

This work was supported by The National Key Research and Development Program of China(2018YFB0605200), National Natural Science Foundation of China (21777047, 51578245), and Scientific Research Project of Guangzhou City (201804020026). We are grateful to Drs. Donald and Karen Barnes for providing helpful advice on our paper.

Appendix A. Supplementary data

Supplementary material related to this article can be found, in the online version, at doi:https://doi.org/10.1016/j.apcatb.2019.118106.

References

[1] L.H. Nie, J.G. Yu, X.Y. Li, B. Cheng, G. Liu, M. Jaroniec, Enhanced performance of NaOH-modified Pt/TiO$_2$ toward room temperature selective oxidation of formaldehyde, Environ. Sci. Technol. 47 (2003) 2777–2783.

[2] J.G. Yu, S.H. Wang, J.X. Low, W. Xiao, Enhanced photocatalytic performance of direct Z-scheme g-C$_3$N$_4$-TiO$_2$ photocatalysts for the decomposition of formaldehyde in air, Phys. Chem. Chem. Phys. 15 (2013) 16883–16890.

[3] IARC, IARC Classifies Formaldehye As Carcinogenic to Humans, Press Releaseno.153, International Agency for Research on Cancer, Lyon, 2004.

[4] S. Weon, J. Kim, W. Choi, Dual-components modified TiO$_2$ with Pt and fluoride as deactivation-resistant photocatalyst for the degradation of volatile organic compound, Appl. Catal. B: Environ 220 (220) (2018) 1–8.

[5] Y.W. Feng, L.L. Ling, J.H. Nie, K. Han, X.Y. Chen, Z.F. Bian, H.X. Li, Z.L. Wang, Self-powered electrostatic filter with enhanced photocatalytic degradation of formaldehyde based on built-in triboelectric nanogenerators, ACS Nano 11 (2017) 12411–12418.

[6] X.B. Zhu, C. Jin, X.S. Li, J.L. Liu, Z.G. Sun, C. Shi, X.G. Li, A.M. Zhu, Photocatalytic formaldehyde oxidation over plasmonic Au/TiO$_2$ under visible light: moisture indispensability and light enhancement, ACS Catal. 7 (2017) 6514–6524.

[7] Y.S. Li, Y. Jiang, S.Q. Peng, F.Y. Jiang, Nitrogen-doped TiO$_2$ modified with NH$_4$F for efficient photocatalytic degradation of formaldehyde under blue light-emitting diodes, J. Hazard. Mater. 182 (2010) 90–96.

[8] J. Zheng, P. Liu, F. Huang, Photocatalytic degradation of volatile organic compounds in an annular reactor under realistic indoor conditions, Environ. Eng. Sci. 32 (2015) 331–339.

[9] S. Xu, Y. Hu, M.M. Zheng, C.H. Wei, Solvent-free in situ synthesis of g-C$_3$N$_4$/ {001}TiO$_2$, composite with enhanced UV- and visible-light photocatalytic activity for NO oxidation, Appl. Catal. B: Environ. 182 (2016) 587–597.

[10] Y. Hu, X. Song, S.M. Jiang, C.H. Wei, Enhanced photocatalytic activity of Pt-doped TiO$_2$ for NOx, oxidation both under UV and visible light irradiation: a synergistic effect of lattice Pt^{4+} and surface PtO, Chem. Eng. J. 274 (2015) 102–112.

[11] F. Quan, Y. Hu, X. Zhang, C.H. Wei, Simple preparation of Mn-N-codoped TiO$_2$ photocatalyst and the enhanced photocatalytic activity under visible light irradiation, Appl. Surf. Sci. 320 (2014) 120–127.

[12] Q.Q. Huang, Y. Hu, G.Y. He, C.J. Lin, C.H. Wei, Photocatalytic oxidation of nitrogen oxides over {001}TiO$_2$: The influence of F$^-$ ions, Environ. Sci. Pollut. Res. 25 (2018) 35342–35351.

[13] S. Miaralipour, D. Friedmann, J. Scott, R. Amal, TiO$_2$/porous adsorbents: recent advances and novel applications, J. Hazard. Mater. 341 (2017) 404–423.

[14] G.F. Guo, Y. Hu, S.M. Jiang, S.H. Wei, Photocatalytic oxidation of NOx over TiO$_2$/ HZSM-5 catalysts in the presence of water vapor: effect of hydrophobicity of zeolites, J. Hazard. Mater. 223–224 (2012) 39–45.

[15] G.Y. He, J.H. Zhang, Y. Hu, Z.G. Bai, C.H. Wei, Dual-template synthesis of mesoporous TiO$_2$ nanotubes with structure-enhanced functional photocatalytic performance, Appl. Catal. B: Environ. 205 (2019) 301–312.

[16] X. Liu, R. Dang, W.J. Dong, X.B. Huang, J. Tang, H.Y. Gao, G. Wang, A sandwich-like heterostructure of TiO$_2$ nanosheets with MIL-100 (Fe): a platform for efficient visible-light-driven photocatalysis, Appl. Catal. B: Environ. 209 (2017) 506–513.

[17] R.R. Liu, J. Wang, J.J. Zhang, S. Xie, X.Y. Wang, Z.J. Ji, Honeycomb-like micro-mesoporous structure TiO$_2$/sepiolite composite for combined chemisorption and photocatalytic elimination of formaldehyde, Microporous Mesoporous Mater. 248 (2017) 234–245.

[18] R. Portela, I. Jansson, S. Suárez, M. Villarroel, B. Sánchez, P. Avil, Natural silicate-TiO$_2$ hybrids for photocatalytic oxidation of formaldehyde in gas phase, Chem. Eng. J. 310 (2017) 560–570.

[19] K. Yamaguchi, K. Inumaru, Y. Oumi, T. Sano, S. Yamanaka, Photocatalytic decomposition of 2-propanol in air by mechanical mixtures of TiO$_2$ crystalline

[20] particles and silicalite adsorbent: the complete conversion of organic molecules strongly adsorbed within zeolitic channels, Microporous Mesoporous Mater. 117 (2009) 350–355.

[20] F. Chen, S.W. Liu, J.G. Yu, Efficient removal of gaseous formaldehyde in air using hierarchical titanate nanospheres with: in situ amine functionalization, Chem. Chem. Phys. 18 (2016) 18161–18168.

[21] G.X. Zhang, A.K. Song, Y.W. Duan, S.L. Zheng, Enhanced photocatalytic activity of TiO$_2$/zeolite composite for abatement of pollutants, Microporous Mesoporous Mater. 255 (2018) 61–68.

[22] T. Luo, J.L. Zhang, W. Li, Z.H. He, X.F. Sun, J.B. Shi, D. Shao, B.X. Zhang, X.N. Tan, B.X. Han, A metal–organic framework-stabilized CO$_2$/water interfacial route for photocatalytic CO$_2$ conversion, ACS Appl. Mater. Interfaces 9 (2017) 41594–41598.

[23] J.X. Xu, J.Y. Gao, C. Wang, Y. Yang, L. Wang, NH$_2$ -MIL-125(Ti)/graphitic carbon nitride heterostructure decorated with NiPd co-catalysts for efficient photocatalytic hydrogen production, Appl. Catal. B: Environ. 219 (2017) 101–108.

[24] Z.H. Rada, H.R. Abid, J. Shang, Y.D. He, P. Webley, S.M. Liu, H.Q. Sun, S.B. Wang, Effects of amino functionality on uptake of CO$_2$, CH$_4$ and selectivity of CO$_2$/CH$_4$ on titanium based MOFs, Fuel 160 (2015) 318–327.

[25] H. Wang, X.Z. Yuan, Y. Wu, G.M. Zeng, H.R. Dong, X.H. Chen, L.J. Leng, Z.B. Wu, L.J. Peng, In situ synthesis of In$_2$S$_3$@MIL-125(Ti) core–shell microparticle for the removal of tetracycline from wastewater by integrated adsorption and visible-light-driven photocatalysis, Appl. Catal. B: Environ. 186 (2016) 19–29.

[26] G. Zhou, M.F. Wu, Q.J. Xing, F. Li, H. Liu, X.B. Luo, J.P. Zou, J.M. Luo, A.Q. Zhang, Synthesis and characterizations of metal-free Semiconductor/MOFs with good stability and high photocatalytic activity for H$_2$ evolution: a novel Z-Scheme heterostructured photocatalyst formed by covalent bonds, Appl. Catal. B: Environ. 220 (2018) 607–614.

[27] I. Ahmed, N.A. Khan, J.W. Yoon, J.S. Chang, S.H. Jhung, Protonated MIL-125-NH$_2$: Remarkable adsorbent for the removal of quinoline and indole from liquid fuel, ACS Appl. Mater. Interfaces 9 (2017) 20938–20946.

[28] H. Liu, J. Zhang, A. Dan, Construction of heterostructured ZnIn$_2$S$_4$@NH$_2$-MIL-125 (Ti) nanocomposites for visible-light-driven H$_2$ production, Appl. Catal. B: Environ 221 (2018) 433–442.

[29] Y.H. Fu, H. Yang, R.F. Du, G.M. Tu, C.H. Xu, F.M. Zhang, M.H. Fan, W.D. Zhu, Enhanced photocatalytic CO$_2$ reduction over Co-doped NH$_2$-MIL-125(Ti) under visible light, RSC Adv. 7 (2017) 42819–42825.

[30] A. Suligoj, U.L. Stangar, A. Ristic, M. Mazaj, D. Verhovsek, N.N. Tusar. TiO$_2$–SiO$_2$ films from organic-free colloidal TiO$_2$ anatase nanoparticles as photocatalyst for removal of volatile organic compounds from indoor air, Appl. Cat. B: Environ. 184 (2016) 119–131.

[31] M. Dan-Hardi, C. Serre, T. Frot, L. Rozes, G. Maurin, C. Sanchez, G. Férey, A new photoactive crystalline highly porous titanium(IV) dicarboxylate, J. Am. Chem. Soc. 131 (2009) 10857–10859.

[32] D.Q. Jin, Q. Xu, L.Y. Yu, X.Y. Hu, Photoelectrochemical detection of the herbicide clethodim by using the modified metal-organic framework amino-MIL-125(Ti)/ TiO$_2$, Microchim. Acta 182 (2015) 1885–1892.

[33] C. Petit, T.J. Bandosz, Synthesis, characterization, and ammonia adsorption properties of mesoporous metal–organic framework (MIL(Fe))–graphite oxide composites: exploring the limits of materials fabrication, Adv. Funct. Mater. 21 (2011) 2108–2117.

[34] L.Y. Qiao, F.Y. Xie, M.H. Xie, C.H. Gong, W.L. Wang, J.C. Gao, Characterization and photoelectrochemical performance of Zn-doped TiO$_2$ films by sol–gel method, Trans. Nonferrous Met. Soc. China 26 (2016) 2109–2116.

[35] S.R. Zhu, P.F. Liu, M.K. Wu, W.N. Zhao, G.C. Ling, K. Tao, F.Y. Yi, L. Han, Enhanced photocatalytic performance of BiOBr/NH$_2$-MIL-125(Ti) composite for dye degradation under visible light, Dalton Trans. 45 (2016) 17521–17529.

[36] D.R. Sun, W.J. Liu, Y.H. Fu, Z.X. Fang, F.X. Sun, X.Z. Fu, Y.F. Zhang, Z.H. Li, Noble metals can have different effects on photocatalysis over metal-organic frameworks (MOFs): a case study on M/NH$_2$-MIL-125(Ti) (M=Pt and Au), Chem. Eur. J. 20 (2014) 4780–4788.

[37] H. Wang, X.Z. Yuan, Y. Wu, G.M. Zeng, X.H. Chen, L.J. Leng, H. Li, Synthesis and applications of novel graphitic carbon nitride/metal-organic frameworks mesoporous photocatalyst for dyes removal, Appl. Catal. B: Environ 174-175 (2015) 445–454.

[38] X.D. Jiang, Y.P. Zhang, J. Jiang, Y.S. Rong, Y.C. Wang, Y.C. Wu, C.X. Pan, Characterization of oxygen vacancy associates within hydrogenated TiO$_2$: a positron annihilation study, J. Phys. Chem. C 116 (2012) 22619–22624.

[39] Z.W. Yang, X.Q. Xu, X.X. Liang, C. Lei, Y.H. Cui, W.H. Wu, Y.X. Yang, Z. Zhang, Z.Q. Lei, Construction of heterostructured MIL-125/Ag/g-C$_3$N$_4$ nanocomposite as an efficient bifunctional visible light photocatalyst for the organic oxidation and reduction reactions, Appl. Catal. B: Environ 205 (2017) 42–54.

[40] B.X. Zhang, J.L. Zhang, X.N. Tan, D. Shao, J.B. Shi, L.R. Zheng, J. Zhang, G.Y. Yang, B.X. Han, MIL-125-NH$_2$@TiO$_2$ core-shell particles produced by a post-solvothermal route for high-performance photocatalytic H$_2$ production, ACS Appl. Mater. Interfaces 10 (2018) 16418–16423.

[41] K. Wei, K.X. Li, L.S. Yan, S.L. Luo, H.Q. Guo, Y.H. Dai, X.B. Luo, One-step fabrication of g-C$_3$N$_4$ nanosheets/TiO$_2$ hollow microspheres heterjunctions with atomic level hybridization and their application in the multi-component synergistic photocatalytic systems, Appl. Catal. B: Environ 222 (2018) 88–98.

[42] Z.Y. Wu, X.B. Huang, H.Y. Zheng, P. Wang, G.T. Hai, W.J. Dong, G. Wang, Aromatic heterocycle-grafted NH$_2$-MIL-125(Ti) via conjugated linker with enhanced

photocatalytic activity for selective oxidation of alcohols under visible light, Appl. Catal. B: Environ 224 (2018) 479–487.

[43] S. Saha, G. Das, J. Thote, R. Banerjee, Photocatalytic metal-organic framework from CdS quantum dot incubated luminescent metallohydrogel, J. Am. Chem. Soc. 136 (2014) 14845–14851.

[44] M.J. Muñoz-Batista, M. de los Milagros Ballari, A. Kubacka, A.E. Cassano, O.M. Alfano, M. Fernández-García, Heterogeneous photocatalysis: light-matter interaction and chemical effects in quantum efficiency calculations, J. Catal. 330 (2015) 154–166.

[45] M.J. Muñoz-Batista, M.M. Ballari, A. Kubacka, O.M. Alfano, M. Fernández-García, Braiding kinetics and spectroscopy in photo-catalysis: the spectro-kinetic approach, J. Am. Chem. Soc. Rev. 48 (2019) 637–682.

[46] M.J. Muñoz-Batista, M. deosMilagros Ballari, A. Kubacka, A.E. Cassano, O.M. Alfano, M. Fernández-García, Acetaldehyde degradation under UV and visible irradiation using CeO2–TiO2 composite systems: Evaluation of the photocatalytic Efficiencies, Chem. Eng. J. 255 (2014) 297–306.

[47] W.A. Saoud, A.A. Assadi, M. Guiza, et al., Abatement of ammonia and butyraldehyde under non-thermal plasma and photocatalysis: oxidation processes for the removal of mixture pollutants at pilot scale, Chem. Engin. J. 344 (2018) 165–172.

[48] W.A. Saoud, A.A. Assadi, M. Guiza, et al., Abatement of ammonia and butyraldehyde under non-thermal plasma and photocatalysis: oxidation processes for the removal of mixture pollutants at pilot scale, Appl. Cat. B: Environ. 213 (2017) 53–61.

[49] W. Elfalleh, A.A. Assadi, A. Bouzaza, D. Wolbert, J. Kiwi, S. Rtimi, Innovative and stable TiO_2 supported catalytic surfaces removing aldehydes under UV-light irradiation, J. Photochem. Photobiol. A: Chem. 343 (2017) 96–102.

[50] X.Y. Li, Y.H. Pi, Q.Q. Hou, H. Yu, Z. Li, Y.W. Li, J. Xiao, Amorphous TiO_2@NH_2-MIL-125(Ti) homologous of-encapsulated heterostructures with enhanced photocatalytic activity, Chem. Commun. (Camb.) 54 (2018) 1917–1920.

[51] M.P. Zhu, Y. Muhammad, P. Hu, B.F. Wang, Y. Wu, X.D. Sun, Z.F. Tong, Z.X. Zhao, Enhanced interfacial contact of dopamine bridged melamine-graphene/TiO_2 nanocapsules for efficient photocatalytic degradation of gaseous formaldehyde, Appl. Catal. B: Environ 232 (2018) 182–193.